Microtubule nucleation promoters Mto1 and Mto2 regulate cytokinesis in fission yeast

Samantha E. R. Dundon[a] and Thomas D. Pollard[a,b,c,*]
[a]Departments of Molecular Cellular and Developmental Biology, [b]Departments of Molecular Biophysics and Biochemistry, and [c]Department of Cell Biology, Yale University, New Haven, CT 06520-8103

ABSTRACT **Microtubules of the mitotic spindle direct cytokinesis in metazoans but this has not been documented in fungi. We report evidence that microtubule nucleators at the spindle pole body help coordinate cytokinetic furrow formation in fission yeast. The temperature-sensitive *cps1-191* strain (Liu *et al.*, 1999) with a D277N substitution in β-glucan synthase 1 (Cps1/Bgs1) was reported to arrest with an unconstricted contractile ring. We discovered that contractile rings in *cps1-191* cells constrict slowly and that an *mto2*^{S338N} mutation is required with the *bgs1*^{D277N}mutation to reproduce the *cps1-191* phenotype. Complexes of Mto2 and Mto1 with γ-tubulin regulate microtubule assembly. Deletion of Mto1 along with the *bgs1*^{D277N} mutation also gives the *cps1-191* phenotype, which is not observed in *mto2*^{S338N} or *mto1*Δ cells expressing *bgs1*$^{+}$. Both *mto2*^{S338N} and *mto1*Δ cells nucleate fewer astral microtubules than normal and have higher levels of Rho1-GTP at the division site than wild-type cells. We report multiple conditions that sensitize *mto1*Δ and *mto2*^{S338N} cells to furrow ingression phenotypes.**

Monitoring Editor
Karen Oegema
University of California, San Diego

Received: Dec 11, 2019
Revised: May 26, 2020
Accepted: Jun 4, 2020

INTRODUCTION

Animals, fungi, and amoebas use an actomyosin contractile ring to divide. Coordinating nuclear division and cytokinesis is required to avoid errors during chromosome segregation, but the mechanisms are incompletely understood.

Cells of the fission yeast *Schizosaccharomyces pombe* assemble a contractile ring from precursors called nodes over 10–15 min following separation of the spindle pole bodies (SPBs) at the onset of anaphase at 23°C (Vavylonis *et al.*, 2008). Furrow ingression starts 35 min after SPB separation (Wu *et al.*, 2003), even if mutations slow the assembly of the ring (Coffman *et al.*, 2009; Roberts-Galbraith *et al.*, 2010; Tebbs and Pollard, 2013; Wang *et al.*, 2014; Laplante *et al.*, 2015). If ring assembly takes longer than 35 min, ingression begins immediately (Chen and Pollard, 2011; Tebbs and Pollard, 2013; Li *et al.*, 2016).

Initiation of furrow ingression by *S. pombe* depends on an intact contractile ring, a signal from the cell cycle clock and septum synthesis. The enzyme β-glucan synthase 1 (Bgs1) concentrates at the equator where it synthesizes the primary septum (Arellano *et al.*, 1996; Cortés *et al.*, 2007) and helps anchor the ring (Arasada and Pollard, 2014; Davidson *et al.*, 2015). Bgs4 (activated by Rho1) and Ags1 (activated by Rho2) synthesize the secondary septum (Arellano *et al.*, 1996; Calonge *et al.*, 2000; Cortés *et al.*, 2005, 2012). Rho1 activity must decrease after septation to allow cell separation (Nakano *et al.*, 1997).

Tension in the ring promotes septum deposition and maintains the circularity of the pore (Thiyagarajan *et al.*, 2015; Zhou *et al.*, 2015), so mutations compromising contractility slow furrow ingression (Pelham and Chang, 2002; Proctor *et al.*, 2012; Tebbs and Pollard, 2013; Laplante *et al.*, 2015; Li *et al.*, 2016). After ~50% ingression, septum synthesis alone can complete division (Proctor *et al.*, 2012). Turgor pressure resists ingression, so mutations that reduce pressure or high osmolarity of the medium favor ingression (Proctor *et al.*, 2012; Morris *et al.*, 2019).

Liu *et al.* (Liu *et al.*, 1999) used chemical mutagenesis to create the *S. pombe* strain *cps1-191* and observed that cells arrested at 36°C with two nuclei and an unconstricted cytokinetic ring. They concluded that colonies did not grow at 36°C due to failed cytokinesis. They found that *cps1*$^{+}$*/bgs1*$^{+}$complemented temperature sensitivity of the strain, identified the D277N substitution in the mutated gene, and named the strain *cps1-191* (Liu *et al.*, 1999). Time-lapse microscopy of the *cps1-191* strain confirmed that the

This article was published online ahead of print in MBoC in Press (http://www.molbiolcell.org/cgi/doi/10.1091/mbc.E19-12-0686) on June 10, 2020.
The authors declare no competing financial interests.
*Address correspondence to: Thomas D. Pollard (thomas.pollard@yale.edu).
Abbreviations used: GDI, GDP-dissociation inhibitor; MTOC, microtubule organizing center; PAA, postanaphase array; SIN, septation initiation network; SPB, spindle pole body.

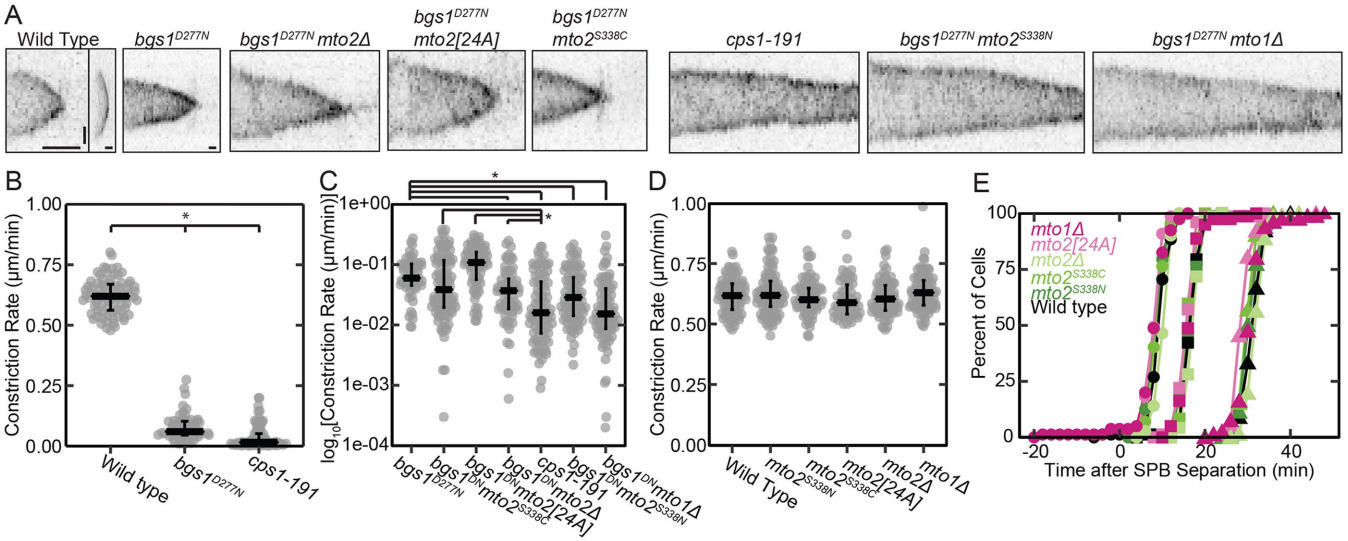

FIGURE 1: Both the *bgs1*^{D277N} and the *mto2*^{S338N} mutations are required to cause the *cps1-191* constriction phenotype in a wild-type background. (A) Kymographs of inverted-contrast, maximum-intensity projected images of contractile rings in strains with Rlc1-tdTomato at 36°C. Wild-type cells were imaged at 1-min intervals, and *bgs1*^{D277N} and *cps1-191* cells were imaged at 5-min intervals. The kymograph of the wild-type cell is displayed (left subpanel) as acquired and (right subpanel) rescaled to match the timescale of the kymographs (other panels) of the *cps1-191* and six different *bgs1*^{D277N} strains. Horizontal scale bars = 15 min, vertical scale bar = 1 μm. (B) Rates of cytokinetic ring constriction measured from a subset of kymographs in A. The data are not normally distributed, so the median and first and third quartiles are indicated by black bars; $n \geq 55$ cells. (C) Log_{10}-transformed cytokinetic ring constriction rates of cells carrying the *bgs1*^{D277N} mutation measured from kymographs as in A. The median and first and third quartiles are indicated by black bars; $n \geq 57$ cells. Significance was determined by Welch's ANOVA followed by a Tukey post-hoc test ($p < 0.05$). (D) Cytokinetic ring constriction rates of cells carrying *bgs1*$^{+}$ measured from kymographs as in A. The median and first and third quartiles are indicated by black bars. No significant differences were detected by Welch's ANOVA. (E) Cumulative distribution plots showing accumulation of cells with rings that have (•) assembled, (■) initiated constriction, and (▲) completed constriction in wild-type and *bgs1*$^{+}$cells with various additional mutations at 36°C. $n \geq 71$ cells for C and D.

nuclei separate normally but actomyosin rings remain intact and unconstricted for an hour at 36°C (Arasada and Pollard, 2014). Many studies have used the *cps1-191* strain to generate cells with nonconstricting actomyosin rings (Pardo and Nurse, 2003; Venkatram *et al.*, 2005; Yamashita *et al.*, 2005; Wachtler *et al.*, 2006; Loo and Balasubramanian, 2008; Roberts-Galbraith *et al.*, 2009; and others).

We found that rings in *cps1-191* cells actually constrict very slowly at 36°C and that cells with the *bgs1*^{D227N} mutation die from lysis rather than cell cycle arrest. Surprisingly, we found that the *cps1-191* constriction phenotype depends on a second point mutation in the gene for the γ-tubulin regulator Mto2, implicating microtubules in the process that drives furrow ingression.

S. pombe has several types of microtubule organizing centers (MTOCs; Sawin and Tran, 2006). During interphase, multiple MTOCs localize along microtubule bundles (Janson *et al.*, 2005). During mitosis, interphase microtubules disassemble and the SPBs nucleate spindle and astral microtubules. During cytokinesis Myp2 recruits MTOCs to the equator (Samejima *et al.*, 2010), where they nucleate the postanaphase array (PAA) of microtubules. These MTOCs depend on Mto1 and, to a lesser extent, Mto2. In the absence of Mto1, no MTOCs form beyond the SPB, which only nucleates microtubules from its inner face (Zimmerman and Chang, 2005). In biochemical experiments, γ-tubulin requires the Mto1/Mto2 complex and MOZART1 homologue Mzt1 to nucleate microtubules (Leong *et al.*, 2019). We find that Mto1/Mto2 complex mutants nucleate fewer astral microtubules and report one consequence: higher than normal Rho1-GTP activity at the cleavage site. Our findings reveal a new link between microtubules and furrow ingression in fission yeast.

RESULTS AND DISCUSSION

Cytokinetic furrows ingress slower in the cps1-191 strain than in cells with the bgs1^{D277N} mutation

Long time-lapse movies at the restrictive temperature of 36°C of the *cps1-191* strain with genome-encoded Rlc1-tdTomato (regulatory light chain for both isoforms of myosin-II, Myo2 and Myp2) revealed that the actomyosin ring constricted ~30-fold slower (median 0.02 μm/min) than in wild-type cells (median 0.62 μm/min; Figure 1, A and B). No rings detached from the plasma membrane (Arasada and Pollard, 2014; Laplante *et al.*, 2015; Cheffings *et al.*, 2019), so Rlc1-tdTomato constriction reflects furrow ingression. Thirty percent of assembled contractile rings slid along the membrane of *cps1-191* cells at 36°C, as reported (Arasada and Pollard, 2014; Cortés *et al.*, 2015). Shifting *cps1-191* cells from the permissive (25°C) to restrictive (36°C) temperature on the microscope showed that more than 30 min at 36°C before SPB separation was required to compromise furrow ingression (Supplemental Figure S1A).

Furrow ingression was threefold faster (median 0.06 μm/min) in a strain with the *bgs1*^{D277N} mutation in a wild-type background than in *cps1-191* cells. Both *bgs1*^{D277N} and *cps1-191* cells have similar growth defects at 36°C, consistent with the 2:2 segregation for this phenotype (Supplemental Figure S1B; Liu *et al.*, 1999). No *bgs1*$^{+}$ cells lysed during imaging, but both *bgs1*^{D277N} and *cps1-191* cells lysed frequently (Supplemental Figure S1D), explaining the growth

Gene	Description	Mutation(s)	Chromosome	Location
tlh1	RecQ type DNA helicase	A1570T	I	5662
nup40	Nucleoporin	T281I	I	1353659
mto2	γ-Tubulin complex linker	S338N	II	494742
cct1	Chaperonin-containing T-complex α-subunit	R269N	II	2307436
SPBC19G7.04	HMG box protein (predicted)	A211V	II	2349593
bgs1	Linear 1,3-β-glucan synthase catalytic subunit	D277N	II	2356243
mae2	Malic enzyme/malate dehydrogenase	D328G, G332D, N131S	III	277211
ers1	RNA-silencing factor	I209L	III	801197

TABLE 1: Mutations in open reading frames in the *cps1-191* strain.

defect at 36°C on solid medium. The lysis frequency varied substantially between replicates, suggesting that this phenotype is sensitive to minute environmental differences. The osmotic stabilizer sorbitol partially rescued the growth of *cps1-191* and *bgs1^{D277N}* cells at 36°C (Supplemental Figure S1C).

The cps1-191 strain carries a large number of mutations

The complete genome sequence of the *cps1-191* strain revealed 384 unique mutations not found in the *S. pombe* reference genome (Wood *et al.*, 2002; Lock *et al.*, 2019). Most (271) were transition mutations as expected from nitrosoguanidine mutagenesis (Supplemental Figure S1E; Balasubramanian *et al.*, 1998). Ten of these transition mutations substituted amino acids in eight genes spanning all three chromosomes, including the reported *bgs1^{D277N}* mutation (Supplemental Figure S1F and Table 1). Two of the eight genes encoding substitutions, *mto2* and *nup40*, have roles in cell cycle regulation or cytokinesis (Lock *et al.*, 2019).

Mutations in the Mto1/Mto2 complex interact synthetically with the bgs1^{D277N} mutation

To determine whether either or both the *mto2* and *nup40* mutations affected the rate of furrow ingression in combination with *bgs1^{D277N}*, we examined multiple progeny from crosses of *cps1-191* strains already confirmed by sequence analysis to contain the *bgs1^{D277N}* mutation. Combining the *bgs1^{D277N}* and *mto2^{S338N}* mutations in a wild-type background reproduced the slow constriction rate of *cps1-191* (Figure 1, A and C, and Supplemental Table S1). Ingression rates of *bgs1^{D277N} nup40^{T281I}*double mutants were no different from *bgs1^{D277N}* alone.

The Mto2 C-terminus is highly phosphorylated (Borek *et al.*, 2015), but neither the *mto2^{S338C}* mutation, which precludes phosphorylation of S338, nor the [24A] strain with 24 phosphorylated serines mutated to alanines (Borek *et al.*, 2015), constricted as slowly as the *bgs1^{D277N} mto2^{S338N}* or *cps1-191* mutants at 36°C (Figure 1, A and C). Cytokinetic rings in both strains were so stable that we never observed one disassemble.

Mto2 regulates MTOCs other than SPBs in *S. pombe* through interactions with its binding partner Mto1 and γ-tubulin (Sawin and Tran, 2006). Neither *mto1*$^+$ nor *mto2*$^+$ are essential genes, but mutations of *mto1*$^+$ are more severe than mutations of *mto2*$^+$ (Sawin *et al.*, 2004; Venkatram *et al.*, 2005). In a *bgs1*$^+$ background with Rlc1-tdTomato to label contractile rings and Pcp1-mEGFP to label SPBs, all mutant strains of *mto1* and *mto2* ingressed furrows at the wild-type rate with cytokinesis timelines similar to wild-type cells (Figure 1, D and E). Deletion of Mto1 in the *bgs1^{D277N}* strain slowed furrowing to the rate observed in *cps1-191* cells, while *bgs1^{D277N} mto2*Δ cells furrowed at an intermediate rate (Figure 1C). Therefore, the *bgs1^{D277N}* mutation sensitizes cells to a compromised Mto1/Mto2 complex. One mechanism might be reduced recruitment of Bgs1 to the division site, but *bgs1*$^+$*mto1*Δ and *bgs1*$^+$*mto2^{S338N}* cells recruited Bgs1 molecules to the equator normally (Supplemental Figure S1G).

The finding that *bgs1^{D277N} mto2^{S338N}* has a more severe phenotype than *bgs1^{D277N} mto2*Δ suggests that the *mto2^{S338N}* mutation may exert a dominant-negative effect on the function of Mto1 that is more severe than the loss of Mto2. We attempted to assess this hypothesis by ectopically introducing the *mto2^{S338N}* coding sequence in addition to the endogenous *mto2*$^+$ gene, but progeny from the crosses exhibited germination defects.

The mto1Δ and mto2^{S338N} mutations disrupt astral microtubules

Wild-type cells nucleated multiple, short-lived astral microtubules from each SPB with a median duration of 20 s (Figure 2A and Supplemental Figure S1H), while *mto2^{S338N}* cells produced fewer astral microtubules and most *mto1*Δ cells nucleated no astral microtubules, as reported (Figure 2, B and C; Sawin *et al.*, 2004). We measured the numbers of microtubules nucleated by SPBs only during anaphase B, to avoid intranuclear "astral" microtubules nucleated earlier (Zimmerman *et al.*, 2004). Immunofluorescence demonstrated similar defects in astral microtubule nucleation in *mto1*Δ and *mto2*Δ cells (Sawin *et al.*, 2004; Janson *et al.*, 2005; Samejima *et al.*, 2005). Furthermore, mitotic spindles reached their maximum lengths and disassembled later than normal in both the *mto2^{S338N}* and *mto1*Δ strains (Figure 2D).

γ-Tubulin-Mto1/Mto2 complexes associated with the cytokinetic ring nucleate PAA microtubules (Samejima *et al.*, 2010). We confirmed that *mto1*Δ cells do not form PAAs (Sawin *et al.*, 2004) but observed that PAA microtubules formed at the normal time in *mto2^{S338N}* cells (Supplemental Figure S1J). This suggested that the loss of astral microtubules, not loss of PAA microtubules, causes a synthetic phenotype with *bgs1^{D277N}*. Experiments with *mto1* mutants that selectively lack either PAA or astral microtubules (Samejima *et al.*, 2010) supported this hypothesis. Only the *mto1(1-1085)* mutant lacking astral microtubules exhibited the synthetic effect on constriction rate when combined with the *bgs1^{D277N}*mutation (Figure 2E).

Astral microtubules may serve as signaling platforms or recruit cell cycle regulators to the SPB, but functions of Mto1 and Mto2 independent of microtubule nucleation may contribute to the synthetic interaction with *bgs1^{D277N}*. To assess this possibility, we tested the effects of depolymerizing microtubules with carbendazim, but microtubules repolymerized within 1 h of continuous exposure to a high dose (250 μg/ml), so insufficient time was available to measure furrow ingression in *bgs1^{D277N}* cells without microtubules.

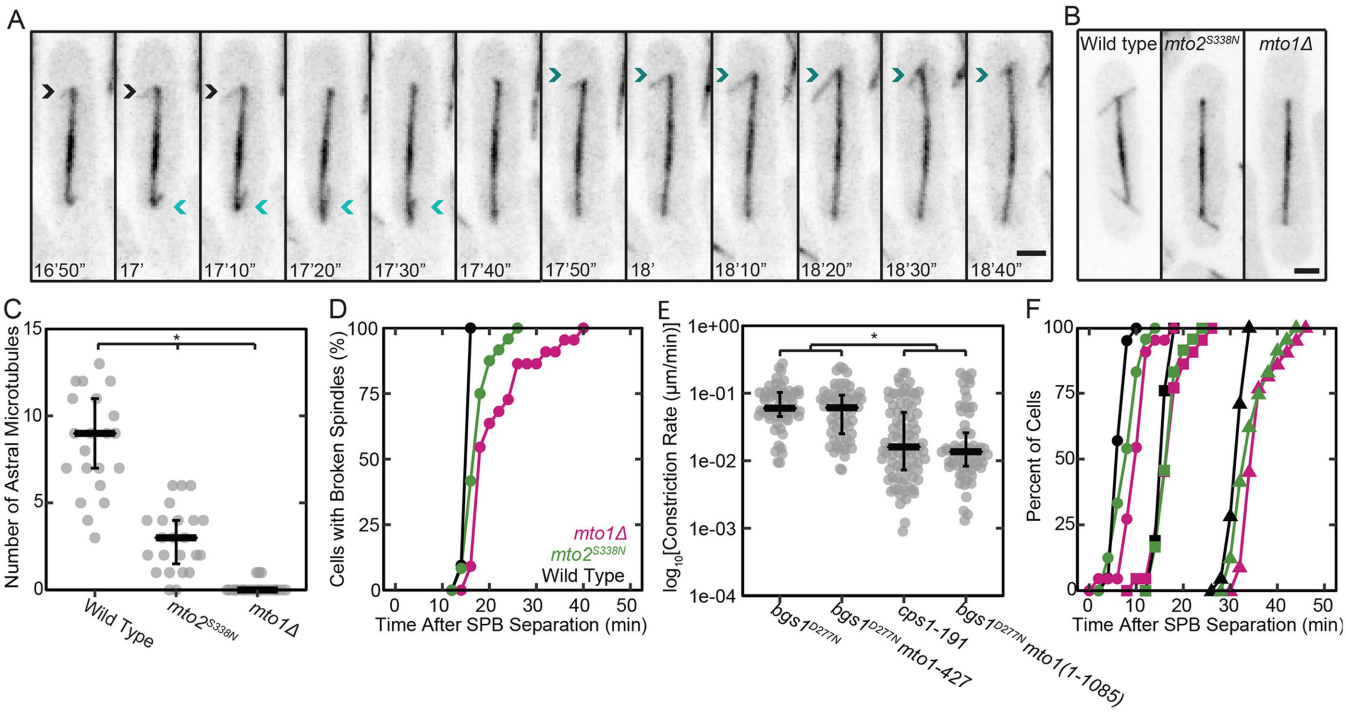

FIGURE 2: The *mto2*^{S338N} and *mto1*Δ mutations perturb astral microtubules and the time of spindle breakage. (A) Time series of inverted-contrast maximum-intensity projected fluorescence micrographs of wild-type cells at 36°C with astral microtubules labeled with GFP-Atb2 (α tubulin). Arrows of the same color mark the same astral microtubule in consecutive frames. Scale bar = 2 μm. (B) Representative fluorescence micrographs of three strains (wild-type, *mto2*^{S338N}, and *mto1*Δ) at 36°C with spindle microtubules labeled with GFP-Atb2. Scale bar = 2 μm. (C) The number of astral microtubules nucleated from a single SPB over the course of mitosis at 36°C in wild-type, *mto2*^{S338N}, and *mto1*Δ cells; $n \geq 21$ spindle poles. Significance was determined using pairwise K-S tests with Bonferroni correction. (D, F) Cumulative distribution plots comparing mitotic and cytokinetic outcomes in wild-type, *mto2*^{S338N}, and *mto1*Δ cells with GFP-Atb2 to mark microtubules, Rlc1-tdTomato to mark the cytokinetic ring, and Sfi1-mCherry to mark SPBs at 36°C; $n \geq 21$ cells. (D) Time course after time zero of the accumulation of cells with broken mitotic spindles, which occurred later than normal in *mto2*^{S338N} and *mto1*Δ strains ($p < 0.05$ by pairwise K-S tests with Bonferroni correction). (E) Log_{10}-transformed cytokinetic ring constriction rates in strains with Rlc1-tdTomato at 36°C lacking either the PAA microtubules (*mto1-427*) or astral microtubules (*mto1(1-1085)*) in combination with *bgs1*^{D277N}. The median and first and third quartiles are indicated by black bars; $n \geq 57$ cells. Significance was determined by Welch's ANOVA followed by a Tukey post-hoc test ($p < 0.05$). (F) Time course after time zero of the accumulation of cells with rings that have (•) assembled, (■) initiated constriction, and (▲) completed constriction. Ring assembly was delayed in cells carrying GFP-Atb2 when combined with the *mto2*^{S338N} and *mto1*Δ mutations but not wild-type cells ($p < 0.05$ by pairwise K-S tests with Bonferroni correction; $n \geq 21$ cells).

Other stresses sensitize cells to mutation of mto1 and mto2

Unconventional type-II myosin *myp2* (Bezanilla *et al.*, 1997; Okada *et al.*, 2019) recruits Mto1 to the ring to generate the PAA (Samejima *et al.*, 2010), and stressing *myp2*Δ cells with 0.6 M KCl delays ring constriction, so we tested whether salt has a similar effect on *mto1*Δ and *mto2*^{S338N} cells. The stress of 0.6 M KCl in minimal medium (EMM5S) had similar effects on wild-type, *mto2*^{S338N}, and *mto1*Δ cells, slowing the time courses of cells completing all three steps in cytokinesis and delaying the onset of ring constriction (Figure 3A), although this delay was less for *mto1*Δ cells than for wild-type and *mto2*^{S338N} cells (Figure 3C). The *mto1*Δ and *mto2*^{S338N} phenotypes differ from the *myp2*Δ phenotype under salt stress (Okada *et al.*, 2019), so the loss-of-function phenotypes differ for the Mto1/Mto2 complex and Myp2. This is further evidence that the PAA is not involved in the phenotype observed in *cps1-191* cells.

Although the cytokinetic timelines of *mto2*^{S338N} and *mto1*Δ cells were indistinguishable from wild-type cells at 36°C (Figure 1E), expression of GFP-tagged α-tubulin (Atb2) in either strain slightly delayed ring assembly but not in wild-type cells (Figure 2F). GFP-tagged α-tubulin also delayed the completion of ring constriction in *mto1*Δ cells, substantiating that additional stressors can perturb cytokinesis in cells with the *mto1*Δ and *mto2*^{S338N} mutations.

The septation initiation network is intact in mto1Δ and mto2^{S338N} cells

The septation initiation network (SIN; Hippo in humans and mitotic exit network in budding yeast) promotes formation of the contractile ring and cytokinesis (Simanis, 2015). High SIN activity can even promote septum formation during interphase (Minet *et al.*, 1979). SPBs are hubs for SIN and other cell cycle signals, and proteins localized to SPBs during mitosis are markers for cell cycle progression (Tatebe *et al.*, 2001; Grallert *et al.*, 2004; Simanis, 2015). Therefore, the loss of astral microtubule nucleation associated with mutations of *mto1* and *mto2* might compromise SIN signaling.

However, our data and the original characterization of *cps1-191* cells (Liu *et al.*, 1999) suggest that the activity of the SIN is normal. Early in mitosis, Cdc7 first localizes to both SPBs and then only one SPB during anaphase B (Sohrmann *et al.*, 1998). Liu *et al.* observed

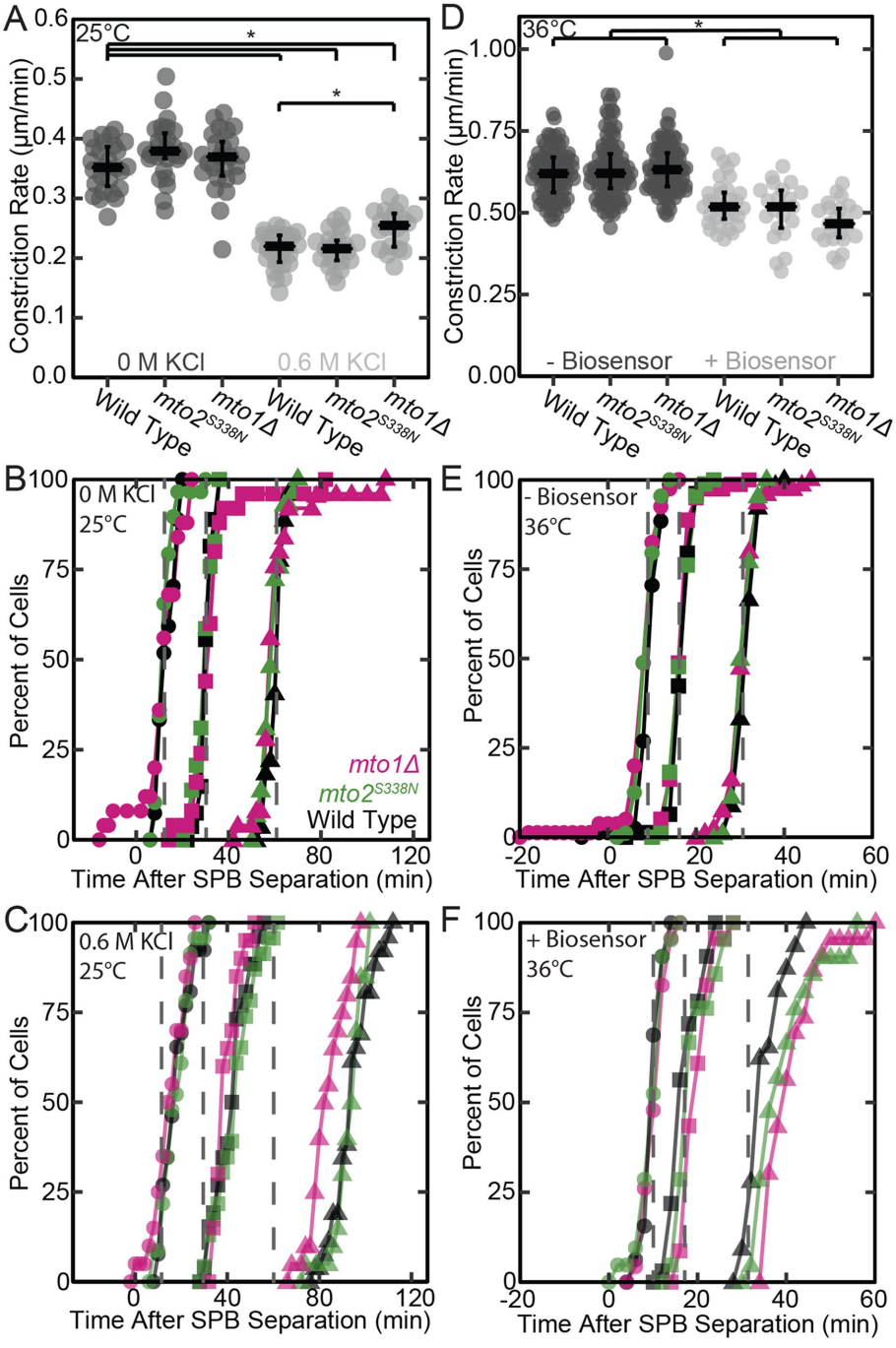

FIGURE 3: The *mto2*^{S338N} and *mto1*Δ mutations sensitize cells to stresses. (A–C) Effects of 0.6 M KCl on cytokinesis in wild-type, *mto2*^{S338N}, and *mto1*Δ cells at 25°C. (A) Rates of cytokinetic ring constriction. The median and first and third quartiles are indicated by black bars and significance ($p < 0.05$) was determined using Welch's ANOVA followed by a Tukey post-hoc test. (B, C) Time courses of cytokinetic events in cells expressing Rlc1-tdTomato to mark the cytokinetic ring and Pcp1-mEGFP to mark SPBs. Cumulative distribution plots show the accumulation of cells with rings that have (•) assembled, (■) initiated constriction, and (▲) completed constriction in medium with (B) no added KCl or (C) 0.6 M KCl. Dashed gray lines in B and C indicate the time when 50% of cells in B reach each milestone to facilitate comparison. $n \geq 20$ cells for A–C. (D–F) Effects of the Rho1-GTP biosensor Pkc1(HR1-C2) on cytokinesis at 36°C. (D) Rates of cytokinetic ring constriction. The median and first and third quartiles are indicated by black bars and significance ($p < 0.05$) was determined using Welch's ANOVA followed by a Tukey post-hoc test. (E, F) Cumulative distribution plots comparing mitotic and cytokinetic outcomes in cells (E) without and (F) with the Pkc1(HR1-C2) Rho1 biosensor. Plots show the accumulation of cells with rings that have with (•) assembled, (■) initiated constriction, and (▲) completed constriction. Dashed gray lines in E and F indicate the time when 50% of cells in F reach each milestone to facilitate comparison. $n \geq 21$ cells for D–F.

the SIN kinase Cdc7 localized to one SPB in cells with an unconstricted ring. Time-lapse imaging showed that the time courses and numbers of Cdc7-mEGFP molecules at each SPB are normal in *mto2*^{S338N} and *mto1*Δ cells (Supplemental Figure S1, K–N).

Contractile rings disassemble before constricting generating multinucleate cells in strains with low SIN activity (Mitchison and Nurse, 1985; Hachet and Simanis, 2008; Dey and Pollard, 2018), but rings never disassembled during our observations of *cps1-191* or *bgs1*^{D277N}*mto2*^{S338N} cells, further evidence that the SIN activity is normal. Interphase *mto2*^{S338N} cells never had two nuclei (0 of 234 cells), and we confirmed this occurs rarely (6 of 220 cells) in *mto1*Δ cells (Zimmerman and Chang, 2005). However, both nuclei can migrate to one side of the contractile ring after it forms at the normal time, creating one half of the cell with two nuclei and the other half lacking nuclei.

Cells lacking Mto1 have altered chromatid cohesion and DNA repair, likely due to loss of nuclear movements dependent on microtubules (Zhurinsky *et al.*, 2019), but it is still unclear how chromosomal abnormalities might be communicated to the division machinery independent of the SIN. Answers should come from research on how microtubules influence prerequisites for furrow formation: an intact contractile ring; a signal from the cell cycle clock; and initiation of septum synthesis.

The concentration of Rho1-GTP at the cleavage site is high in mto1Δ and mto2^{S338N} cells

To explore one pathway that might be influenced by defects in astral microtubules, we localized *S. pombe* Rho1-GTP using the Pkc1(HR1-C2)-mEGFP biosensor (Davidson *et al.*, 2015). This probe, derived from *Saccharomyces cerevisiae* Pkc1, contains Rho1-GTP binding HR1 domains and a plasma-membrane targeting C2 domain fused to mEGFP (Kono *et al.*, 2012). Active GTP-bound RhoA concentrates in the cell cortex of metazoan cells (Michaelson *et al.*, 2001) through the C-terminal CAAX motif, which is thought to promote activation by GEFs.

The fluorescence of this probe is the same when free or bound to Rho1-GTP, so it can measure local accumulation but not the total active Rho1-GTP. Binding of biosensors can compromise functions of the target protein, so expression of the biosensor may perturb cytokinesis if Rho1-GTP regulates furrow formation. Therefore, we expressed Pkc1(HR1-C2)-mEGFP from the thiamine-repressible *3nmt1* promoter in medium lacking thiamine (i.e., inducing conditions)

for only ~15 h before imaging, the minimum time for maximum expression (Maundrell, 1990). Conveniently, expression from the *P3nmt1* promoter was highly variable, giving cells with a range of concentrations of Pkc1(HR1-C2)-mEGFP.

Expression of the biosensor did not affect the time course of contractile ring assembly or constriction rate at 36°C of wild-type, *mto2*^{S338N}, or *mto1*Δ cells, but delayed the times when populations of these cells initiated and completed ring constriction (Figure 3, D–F). The populations of *mto2*^{S338N} and *mto1*Δ cells completed ring constriction later than wild-ype cells expressing the biosensor (Figure 3F). Pkc1(HR1-C2) expression levels were not normally distributed, so we used a Spearman correlation test to show that constriction rates were not strongly correlated with Pkc1(HR1-C2) level (Supplemental Figure S1I).

Pkc1(HR1-C2)-mEGFP concentrates at growing cell tips during interphase and at the cytokinetic furrow at 36°C (Figure 4, A and B, and Supplemental Movie S1) as reported at 25°C (Davidson *et al.*, 2015). However, at 36°C the fraction of cells with Pkc1(HR1-C2)-mEGFP concentrated at one or both ends was higher in wild-type than in mto2^{S338N} and mto1Δ mutant cells (Figure 4D). Poor growth of *bgs1*^{D277N} cells expressing Pkc1(HR1-C2)-mEGFP at 36°C precluded localization of GTP-Rho1. Ectopic concentration of Pkc1(HR1-C2)-mEGFP at other cortical locations was more frequent in *mto2*^{S338N} (49%) and *mto1*Δ (46%) mutants than wild-type (23%) cells (Figure 4C and Supplemental Movie S1), especially in cells with low concentrations at their poles (Figure 4D). Thus, Pkc1(HR1-C2)-mEGFP compromises some cellular functions and *cps1-191* cells are particularly sensitive.

The Pkc1(HR1-C2)-mEGFP signal at the cleavage site peaked during furrow ingression (Figure 4C), followed by a brief decrease and second peak during cell separation (single light-blue data point in Figure 4C). The normalized peaks of Pkc1(HR1-C2)-mEGFP fluorescence during cytokinesis and at separation were more intense in *mto2*^{S338N} and *mto1*Δ cells than in wild-type cells (Figure 4D). Furthermore, the peak of Pkc1(HR1-C2)-mEGFP fluorescence during cytokinesis was prolonged in *mto1*Δ cells (Figure 4E). Nevertheless, the timing of cytokinesis was normal in *mto1*Δ and *mto2*^{S338N} cells relative to mitotic events (Figure 1E). An additional insult (e.g., *bgs1* mutation, salt stress, Rho1 biosensor, or GFP-Atb2 expression) is required to sensitize these cells and generate a phenotype. More work is required to assess which Rho1 regulators contribute to the observed hyperactivation, how microtubules regulate any of these proteins, and to determine how high Rho1 accumulation influences furrow ingression.

Excess Rho1-GTP may compromise the activities of other GTPases through a mechanism involving GDP-dissociation inhibitors (GDIs). The *bgs1*^{D227N} mutation in the wild- type background slows furrow ingression by 90%, and combining the *bgs1*^{D227N} mutation with *mto1* or *mto2* mutations slows furrowing another threefold in spite of normal Bgs1 recruitment to the division site in *mto2*^{S338N} and *mto1*Δ cells. The abnormally thick cell walls and secondary septa in cells depleted of Bgs1 and *cps1-191* cells suggest that other glucan synthases are overactive to compensate for the loss of Bgs1 activity (Cortés *et al.*, 2007, 2015; Sethi *et al.*, 2016). In mammalian cells, small GTPases (e.g., Rho, Rac, Cdc42) compete for GDIs, so changes in RhoA activity can affect other GTPases (Boulter *et al.*, 2010). *S. pombe* has a single Rho GDI, Gdi1, so high Rho1-GTP at the division site of *bgs1*^{D277N}, *mto2*^{S338N}, or *bgs1*^{D277N} *mto1*Δ cells may release Gdi1 to interact with other GTPases involved in cytokinesis such as Rho2, which stimulates Ags1 to synthesize the secondary septum. Reducing GTP-Rho2 would compromise the ability of Ags1 to compensate for low Bgs1 activity.

CONCLUSIONS

For two decades, the *cps1-191* strain has been used to generate *S. pombe* cells arrested with unconstricting actomyosin rings. We find that this phenotype depends on both the originally identified *bgs1*^{D277N} mutation and the *mto2*^{S338N} mutation. Caution is advised when interpreting experiments on *cps1-191* cells that examine the "arrest" phenotype, particularly if the *cps1-191* strain is crossed with other strains. The *bgs1* and *mto2* loci are ~2 Mb apart on chromosome II, and we frequently observed recombination events between these genes, so the two mutations can be separated.

Our work demonstrates cross-talk between the proteins that nucleate astral microtubules and the machinery driving furrow ingression. Compromising this communication results in excess active Rho at the cleavage site. RhoA determines the division site in metazoan cells by activating formins to assemble actin filaments, stimulating Rho-associated protein kinase to activate myosin-II, and promoting midbody ring maturation through citron kinase (Pollard, 2017; El-Amine *et al.*, 2019). Other mechanisms position cytokinetic rings in *S. pombe* (Pollard, 2017), but Rho1 contributes to full activation of the SIN to drive ring formation (Alcaide-Gavilán *et al.*, 2014) and activates glucan synthases to form the septum (Arellano *et al.*, 1996). Thus, Rho signaling is an ancient mechanism to coordinate cytoskeletal elements, but it has been adapted for a range of functions to regulate cytokinesis during the divergence from the last eukaryote common ancestor.

METHODS AND MATERIALS

Growth conditions and strain construction

Supplemental Table S2 lists the *S. pombe* strains used in this work. Oligonucleotide primers were from Millipore Sigma. Restriction enzymes were from New England BioLabs. Plasmid purification was performed using an E.Z.N.A. Plasmid Mini Kit (Omega Bio-tek) with Miraprep modifications (Pronobis *et al.*, 2016). The Keck DNA Sequencing Lab of Yale University performed routine DNA sequencing. All cloning was done with high-efficiency NEB 5-alpha Competent *Escherichia coli* from New England BioLabs. Standard methods were used for genetic crosses (Moreno *et al.*, 1991).

mto2^{S338N}*:KanMX6* and *mto2*^{S338C}*:KanMX6* strains of *S. pombe* were generated by homologous integration (Bähler *et al.*, 1998). First, pFA6a-mto2^{S338N}-C-KanMX6 was generated. A 245-base fragment of the end of the *mto2* coding sequence was amplified from *cps1-191* (containing the *mto2*^{S338N} mutation) with flanking homology to the pFA6a vector using the Expand High Fidelity PCR system (Millipore Sigma). The vector backbone was amplified from pFA6a-GFP-KanMX6 using Phusion polymerase (New England BioLabs). Both PCR reactions were digested with *Dpn*I and purified using an E.Z.N.A. Cycle Pure Kit (Omega Bio-tek). pFA6a-mto2^{S338N}-C-KanMX6 was generated using NEBuilder HiFi DNA Assembly Master Mix (New England BioLabs) in an assembly containing 5 fmol of each fragment. The *mto2*^{S338N} segment was verified by sequencing. pFA6a-mto2^{S338C}-C-KanMX6 was generated by site-directed mutagenesis. Mutagenic primers were used to amplify pFA6a-mto2^{S338N}-C-KanMX6 using the Expand High Fidelity PCR system (Millipore Sigma). The PCR product was digested with *Dpn*I and transformed into NEB 5-alpha Competent *E. coli*. The *mto2*^{S338C}segment was verified by sequencing.

PCR-based homologous integration cassettes were amplified using the Expand High Fidelity PCR system (Millipore Sigma) from the appropriate plasmid with 80 base pairs flanking homology to replace the 3′ end of *mto2* (primers designed with PPPP at www.bahlerlab.info/resources/; Bähler *et al.*, 1998). Lithium acetate transformation was used to introduce 5–10 μg of integration

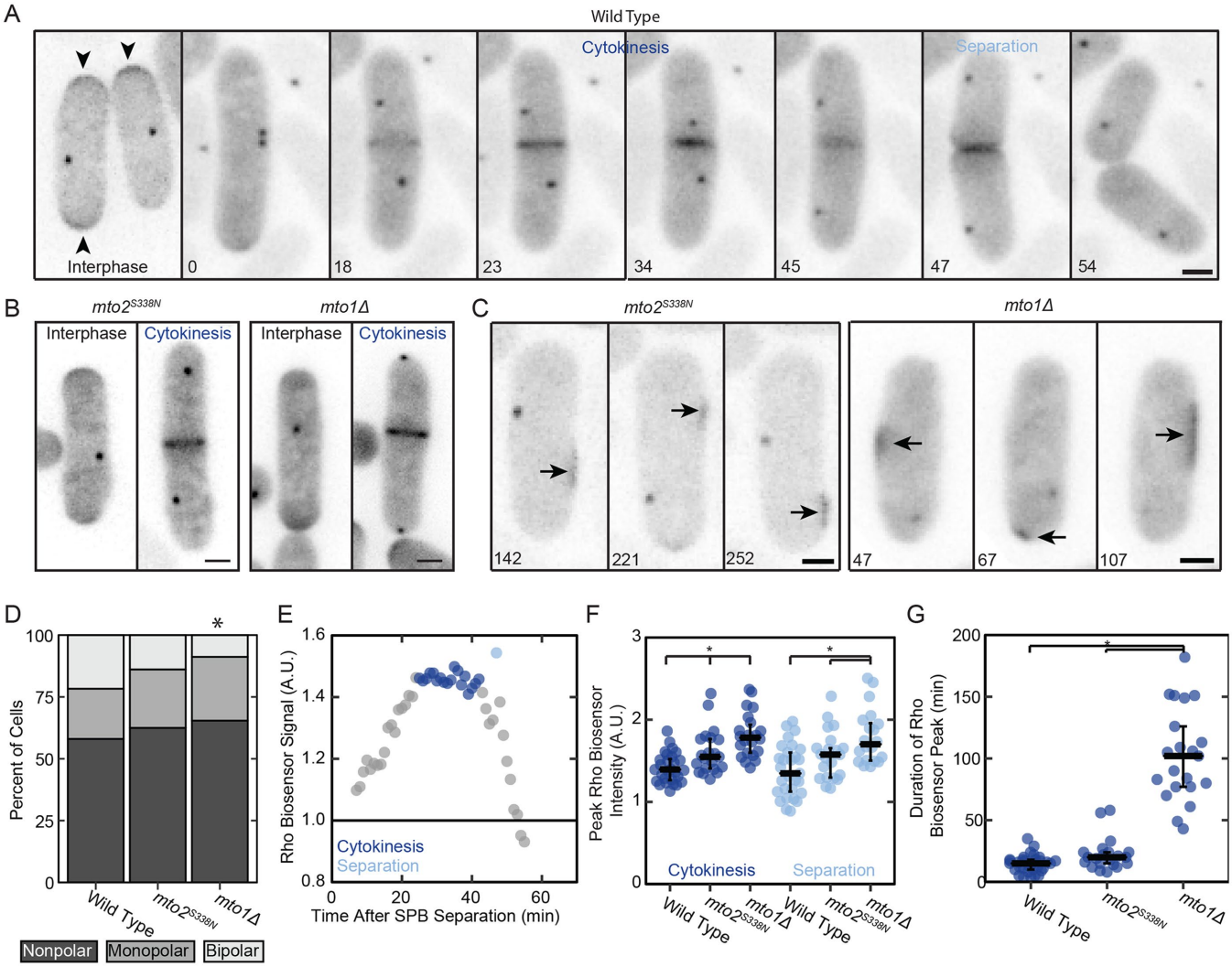

FIGURE 4: The *mto2*^{S338N} and *mto1*Δ mutations disrupt Rho1 signaling. (A–C) Inverted-contrast maximum-intensity projected fluorescence micrographs of cells at 36°C expressing the Rho1 biosensor Pkc1(HR1-C2)-mEGFP and Pcp1-mEGFP to mark SPBs. Scale bars 2 µm. (A) Wild-type cells. Active Rho1 concentrates at poles of interphase cells (arrowheads) and at the equator of cells during cytokinesis and septation. Times are minutes after SPB separation. (B) *mto2*^{S338N} and *mto1*Δ cells exhibiting Rho1 concentration at cell ends during interphase (each left) and cell equators during cytokinesis (each right). (C) Representative images of *mto1*Δ and *mto2*^{S338N} cells during interphase showing fluctuating, ectopic concentrations of the biosensor (arrows) at times denoted in minutes after the start of image acquisition. Ectopic accumulations were observed in 23% of wild-type, 49% of *mto2*^{S338N}, and 46% of *mto1*Δ cells; $n \geq 72$ cells; $p = 0.007$ and 0.006, respectively, from the wild-type population by a chi-squared test with Bonferroni correction for multiple comparisons. (D) The percent of cells exhibiting bipolar, monopolar, or nonpolar growth in an asynchronous population of cells expressing Pkc1(HR1-C2)-mEGFP shifted to 36°C. Asterisk denotes significant difference ($p = 0.008$) from the wild type as determined by a chi-squared test with Bonferroni correction for multiple comparisons; $n \geq 143$ cells. (E) Time course of the integrated density of the Rho1 biosensor at the equator of the cell in A during cytokinesis normalized to interphase value. The main peak (dark blue) is during furrow formation and the short second peak (light blue) is at cell separation. (F, G) Rho1 biosensor signals at the equators of populations of ≥21 cells. Significance ($p < 0.05$) was determined using Welch's ANOVA and Tukey's post-hoc analysis. (F) Peak Rho1 biosensor signal at the equator during cytokinesis and separation. (G) Duration of Rho1 biosensor peak during cytokinesis.

cassette DNA (Murray *et al.*, 2016). Integration at the correct locus was verified by colony PCR using LongAmp *Taq* 2X Master Mix (New England BioLabs), and the *mto2* gene was sequenced in its entirety to verify the S338N or S338C point mutations.

The *bgs1*^{D277N} strain was generated by CRISPR (Fernandez and Berro, 2016). A two-step PCR was used to assemble pUR19-adh1-Cas9-rrk1-sgRNA:Fex1^{+} with a guide sequence targeting *bgs1* using Q5 High-Fidelity polymerase (New England BioLabs). pUR19-adh1-Cas9-rrk1-sgRNA:Fex1^{+} and a 400–base pairs repair guide fragment containing the *bgs1*^{D277N} mutation were introduced into *fex1*Δ *fex2*Δ *S. pombe* cells by lithium acetate transformation (Murray *et al.*, 2016). The *bgs1* gene was sequenced in its entirety to verify the *bgs1*^{D277N} mutation.

For serial dilution assays, 10-ml cultures of each strain were maintained in exponential phase for 36 h in YE5S (rich) medium in 50-ml baffled flasks. All cultures were diluted to an OD_{595} of 0.5. Five 10-fold serial dilutions were made for each strain, yielding a total of six cellular densities. Five microliters of each concentration was

spotted on YE5S + 1.8% agar or YE5S 1.2 M sorbitol + 1.8% agar plates. Each plate was grown either at 25°C or 36°C and imaged each day for 4 d to monitor growth.

Whole-genome sequencing

S. pombe genomic DNA was isolated using a *Quick*-DNA Fungal/Bacterial Miniprep kit and purified by a Genomic DNA Clean & Concentrator-25 kit (both from Zymo Research). Genomic DNA was sequenced on a NovaSeq 6000 (Illumina) with 150–base pairs paired reads at the Yale Center for Genome Analysis. Sequence data quality was examined using FastQC v 0.11.7 (Babraham Bioinformatics). The *S. pombe* reference genome was downloaded from PomBase (Lock *et al.*, 2019) and reads were aligned using MagicBLAST (Zhang *et al.*, 2015). Aligned reads were sorted, duplicates removed, and indexed using SAMtools (Li *et al.*, 2009). Deviations from the reference genome were identified using Pilon (Walker *et al.*, 2014), and alignments were viewed using IGV 2.4.10 (Robinson *et al.*, 2017). Identified mutations were cross-referenced with PomBase to determine location, eliminate previously-reported variants, and identify protein-coding mutations (Lock *et al.*, 2019).

Microscopy

Cells were grown in 50-ml baffled flasks in exponential phase at 25°C in YE5S (rich) medium for 24 h, then washed in EMM5S (low-fluorescence) medium for an additional 12 h. For experiments at 36°C, the culture was shifted to 36°C 2 h before mounting and imaging. To image, cells were isolated by centrifugation at 2300 × *g* for 30 s, washed with fresh EMM5S, and resuspended at ~20-fold higher concentration than in culture. Then 1.5–2.0 µl of concentrated cells were mounted on an EMM5S + 2% agarose pad freshly poured on a Therminator block (Davies *et al.*, 2014) and a 24 × 50 mm no. 1.5 coverslip was applied (Globe Scientific). Then 150 µl of EMM5S was injected beneath the coverslip in contact with the agarose pad and the edges of the chamber were sealed using VALAP to reduce shrinkage of the pad. For salt stress experiments, cells at 25°C were washed and resuspended in EMM5S + 0.6 M KCl, then immediately mounted on an EMM5S + 0.6 M KCl + 2% agarose pad on a Therminator block and imaged at 25°C. The average time between KCl addition and initiation of imaging was 5 min.

Cells were visualized using an Olympus IX-71 microscope with a 100×/ NA 1.4 Plan Apo lens (Olympus) and a CSU-X1 (Andor Technology) confocal spinning-disk confocal system equipped with an iXON-EMCCD camera (Andor Technology). OBIS 488-nm LS 20 mW and OBIS 561-nm LS 20 mW lasers (Coherent) were used for excitation. The desired temperature was maintained during acquisition using a home-built version of the Therminator (Davies *et al.*, 2014). Images were acquired using Micromanager 1.4 (Edelstein *et al.*, 2014).

Acquisition settings for Pcp1-mEGFP Rlc1-tdTomato: 12 Z-slices were acquired with 0.5 µm spacing; 22 µW, 561 nm laser power and 50-ms exposures; 35 µW, 488 nm laser power and 50-ms exposures (power measured at the objective). An emission filter suitable for both tdTomato and mEGFP fluorescence was used to reduce the number of filter changes. All *bgs1*$^{+}$cells were imaged at 4 XY positions and 1-min intervals. Cells carrying *bgs1*^{D277N} were imaged at 20 XY positions and 5-min intervals.

Acquisition settings for Rlc1-tdTomato Sfi1-mCherry mEGFP-Atb2: For cytokinesis timelines to determine the timing of spindle breakage, 12 Z-slices were acquired with 0.5 µm spacing at three XY positions and 1-min intervals using 150-ms exposures with 32 µW, 561 nm laser power, and 200-ms exposures with 89 µW, 488 nm laser power at the objective. Separate emission filters were used for tdTomato/mCherry and mEGFP fluorescence to avoid bleedthrough of the fluorophores with different spectral characteristics. To measure astral microtubule numbers and longevities, only mEGFP-Atb2 was imaged using 89 µW, 488 nm laser power and 200-ms exposures of 10 Z-slices with 0.5 µm spacing at one XY position at 10-s intervals.

Acquisition settings for GFP-Bgs1 Rlc1-tdTomato Sfi1-mCherry: 12 Z-slices with 0.5 µm spacing were acquired at three XY positions and 1-min intervals using 150-ms exposures with 32 µW, 561 nm laser power, and 100-ms exposures with 89 µW, 488 nm laser power at the objective. Separate emission filters were used for tdTomato/mCherry and mEGFP fluorescence to avoid bleedthrough of the fluorophores with different spectral characteristics. Strains bearing GFP-tagged proteins for the calibration curve were imaged under identical conditions. For camera noise correction, 100 images were acquired with 100-ms exposures and the shutter closed; for uneven illumination correction, dilute fluorescein was mounted on a 2% agarose EMM5S pad on the Therminator and 100 images were acquired using 50-ms exposures with 34 µW, 488 nm laser power.

Image analysis

All image visualization and analyses were done using Fiji (Schindelin *et al.*, 2012). Macros used for processing can be downloaded from https://github.com/SDundon/ImageJ-Processing-Macros. Before analysis, the contrast of each image was adjusted so that the black point was 5% below extracellular background signal and the white point was 20% above maximum signal intensity. Representative images were selected based on similarity to median values of each data set.

Constriction rates and cytokinesis timeline measurements: Maximum-intensity projections were produced for each time-lapse acquisition and a kymograph was first produced for each ring. If necessary, the StackReg plugin (Thévenaz *et al.*, 1998) was used to register images across all time points. A line was drawn parallel to the ring, the "reslice" tool in Fiji used, and the resliced image was maximum-intensity projected to create a kymograph. The ring circumference for each time point was calculated using the 180912_AutoCircum.ijm macro. Circumference was plotted against time as a scatter plot in Microsoft Excel, and a linear trendline fit to the slope to calculate the constriction rate. For analysis of cells bearing the *bgs1*^{D277N} mutation (including *cps1-191*), cells were excluded from analysis if SPB separation occurred more than 2 h after the start of acquisition. We found that rings formed after this time always constricted at an even slower rate, most likely due to effects of phototoxicity.

Cytokinesis milestones were defined as follows: "SPB separation" is the first frame in which two SPBs labeled with Pcp1-mEGFP could be resolved; "Complete assembly" is the first frame in which no Rlc1-tdTomato–labeled nodes were visible adjacent to the ring, because all had coalesced at the equator; "Constriction onset" is the first frame in which the Rlc1-tdTomato–labeled ring was smaller than its initial diameter and continued to decrease in size; "Constriction complete" is the frame in which the Rlc1-tdTomato signal reached its smallest size at the end of constriction. All milestones were temporally aligned with SPB separation set as time 0 and plotted as cumulative distributions. Spindle breakage was defined as the first time point in which there was no longer a single microtubule structure marked with GFP-Atb2 connecting the two SPBs. PAA appearance was defined as the first frame in which microtubules appeared at the equator distinct from the mitotic spindle.

Astral microtubule measurements: Astral microtubules were considered to be the same structure across consecutive frames (10-s intervals) if they 1) originated from the same SPB and 2) were

oriented in the same direction ±45° relative to the SPB in consecutive frames (Figure 3A). The number of astral microtubules that originated from a single SPB during anaphase B was determined to exclude the intranuclear "astral" microtubules that form during earlier phases of mitosis (Zimmerman *et al.*, 2004).

Rho biosensor and GFP-Bgs1 measurements: A region of interest (ROI) was selected for bleach correction reference using the following criteria: 1) must stay within the boundaries of one cell for the duration of the acquisition; 2) must be located within a cell that does not divide for the duration of the movie (to prevent differences in cytosolic concentration due to recruitment to the division site); and 3) Pcp1-mEGFP–marked SPB must never enter the ROI. The same ROI was used for bleach correction of all channels. Bleach correction was conducted using the Fiji plugin for Exponential Fitting Method for the Bleach Correction. The intensity from all 12 Z-slices (0.5 µm apart) was then summed.

Rho biosensor measurements: Before analysis, the contrast of each image was adjusted so that the black point was 5% below extracellular background signal and the white point was 20% above maximum signal intensity of Pcp1-mEGFP, which was more consistent than Pkc1(HR1-C2)-mEGFP signal. As previously observed, expression from the *3nmt1* promoter was highly variable. Therefore, cells were analyzed that had an average Pkc1(HR1-C2)-mEGFP pixel intensity of more than 175,000 A.U. (arbitrary units) at SPB separation. This was calculated by drawing a spline-fit polygon ROI around the cell at the last time point before SPB separation. The integrated density was measured for this ROI, as well as a circular ROI covering the SPB (Supplemental Figure S1O). The SPB integrated density was subtracted from the cellular integrated density, and this value divided by the cell area with SPB area subtracted. This value (175,000 A.U.) was selected because cells of all genotypes below this threshold were found to have very low peak Rho/interphase Rho ratio values with a very different SD than cells above this threshold. We reasoned that cells below this threshold express insufficient Pkc1(HR1-C2)-mEGFP to enable reliable measurement of Rho1-GTP enrichment at the cell equator. After elimination of cells below this threshold, the data were homoscedastic when the ratio was plotted against average pixel intensity.

To determine cellular polarity, a cell end was counted as "polarized" if it exhibited visible Pkc1(HR1-C2)-mEGFP enrichment and/or was observed to grow over the course of the time-lapse experiment. Cells that exhibited no growth from either end were scored as "nonpolar," growth from one end was scored as "monopolar," and growth from both ends was "bipolar." Cells undergoing cytokinesis were excluded from this analysis, as cell ends cease growth during this time.

To calculate the peak Rho/interphase Rho ratio, a 3.75 × 1.95 µm ROI was positioned with the cytokinetic ring in the center (long axis to match the cell width; Supplemental Figure S1O). The integrated density was measured for this ROI for each time point. These values were divided by the integrated density of this ROI for the time point immediately before SPB separation to normalize the intensity by Pkc1(HR1-C2)-mEGFP expression. Normalized intensity was plotted against time using Microsoft Excel; all time points in which the SPB was located within the ROI were excluded (Figure 3E). To measure peak duration, the peak fluorescence start was defined as the last time point of consistent signal increase across more than three time points. Peak end was defined as the last time point before consistent signal decrease below the peak start value across more than three time points. For cytokinesis peak signal, the maximum ratio between these points was determined. For separation peak signal, the maximum normalized signal within two time points of cell separation was determined.

Measurements of Bgs1 and Cdc7 molecule numbers: Bleach-corrected summed intensity images were corrected for camera noise and uneven illumination. To generate the calibration curve, a spline-fit polygon ROI was drawn around wild-type (unlabeled) cells and the average intensity in the ROI was measured (n = 74 cells). Subsequently, ROIs were similarly drawn around cells bearing seven different GFP-tagged proteins for the calibration curve (n > 65 cells). For each cell, the wild-type background fluorescence was subtracted and the integrated density was calculated. These integrated density measurements were plotted against the average number of molecules per cell for each protein reported in Wu and Pollard, 2005 and fit with a linear regression (Wu and Pollard, 2005).

For Bgs1: A 1.0 µm × 3.75 µm (cell width) ROI was positioned to cover the equatorial GFP-Bgs1 signal and the integrated density measured from cell cycle time zero until 30 min past the completion of constriction. The same ROI was used to measure cytoplasmic GFP-Bgs1 signal adjacent to the ring at constriction onset. Cytoplasmic GFP-Bgs1–integrated density was subtracted from the equatorial signal until the onset of constriction. The average constriction rate and average ring size were used to calculate a correction factor for the progressively smaller cytoplasmic volume within the plane of the constricting ring, which was applied to the value of the cytoplasmic signal and subtracted from the equatorial signal until constriction completion.

For Cdc7: A 1.0 µm ×1.0 µm ROI was positioned over each SPB, and the integrated density measured from the first time point where signal was visible above background (typically at SPB separation as determined by Sfi1-mCherry signal). The same ROI was used to measure cytoplasmic Cdc7-mEGFP at SPB separation, and this was subtracted from the signal measurements to correct for the large volume of cytoplasm not containing the SPB.

Statistical analysis

All statistical tests were carried out in R (R Core Team, 2018). Plotting was done using tidyverse and ggbeeswarm packages (Clarke and Sherrill-Mix, 2017; Wickham, 2017), except for pie charts in Figure 2, which were generated using Microsoft Excel.

ACKNOWLEDGMENTS

Research reported in this publication was supported by National Institute of General Medical Sciences of the National Institutes of Health under award no. R01GM026132 and an NRSA fellowship (F32GM125193) to S.D. The authors thank M. Balasubramanian, M. Das, and D. McCollum, for useful discussions; F. Chang, M. C. King, J. C. Ribas, K. E. Sawin, and J.-Q. Wu for generously sharing *S. pombe* strains; J. Berro and R. Fernandez for assistance with CRISPR; and R. M. Dundon and T. J. Straub for assistance with genome analysis. The content is solely the responsibility of the authors and does not necessarily represent the official views of the National Institutes of Health.

REFERENCES

Alcaide-Gavilán M, Lahoz A, Daga RR, Jimenez J (2014). Feedback regulation of SIN by Etd1 and Rho1 in fission yeast. Genetics 196, 455–470.

Arasada R, Pollard TD (2014). Contractile ring stability in *S. pombe* depends on F-BAR protein Cdc15p and Bgs1p transport from the Golgi complex. Cell Rep 8, 1533–1544.

Arellano M, Durán A, Pérez P (1996). Rho 1 GTPase activates the (1-3)β-D-glucan synthase and is involved in *Schizosaccharomyces pombe* morphogenesis. EMBO J 15, 4584–4591.

Bähler J, Wu JQ, Longtine MS, Shah NG, McKenzie A, Steever AB, Wach A, Philippsen P, Pringle JR (1998). Heterologous modules for efficient and versatile PCR-based gene targeting in *Schizosaccharomyces pombe*. Yeast 14, 943–951.

Balasubramanian MK, McCollum D, Chang L, Wong KC, Naqvi NI, He X, Sazer S, Gould KL (1998). Isolation and characterization of new fission yeast cytokinesis mutants. Genetics 149, 1265–1275.
Bezanilla M, Forsburg SL, Pollard TD (1997). Identification of a second myosin-II in *Schizosaccharomyces pombe*: Myp2p is conditionally required for cytokinesis. Mol Biol Cell 8, 2693–2705.
Borek WE, Groocock LM, Samejima I, Zou J, de Lima Alves F, Rappsilber J, Sawin KE (2015). Mto2 multisite phosphorylation inactivates non-spindle microtubule nucleation complexes during mitosis. Nat Commun 6, 1–16.
Boulter E, Garcia-Mata R, Guilluy C, Dubash A, Rossi G, Brennwald PJ, Burridge K (2010). Regulation of Rho GTPase crosstalk, degradation and activity by RhoGDI1. Nat Cell Biol 12, 477–483.
Calonge TM, Nakano K, Arellano M, Arai R, Katayama S, Toda T, Mabuchi I, Pérez P (2000). *Schizosaccharomyces pombe* Rho2p GTPase regulates cell wall α-glucan biosynthesis through the protein kinase Pck2p. Mol Biol Cell 11, 4393–4401.
Cheffings TH, Burroughs NJ, Balasubramanian MK (2019). Actin turnover ensures uniform tension distribution during cytokinetic actomyosin ring contraction. Mol Biol Cell 30, 933–941.
Chen Q, Pollard TD (2011). Actin filament severing by cofilin is more important for assembly than constriction of the cytokinetic contractile ring. J Cell Biol 195, 485–498.
Clarke E, Sherrill-Mix S (2017). Categorical scatter (Violin point) plots [R package ggbeeswarm version 0.6.0].
Coffman VC, Nile AH, Lee I-J, Liu H, Wu J-Q (2009). Roles of formin nodes and myosin motor activity in Mid1p-dependent contractile-ring assembly during fission yeast cytokinesis. Mol Biol Cell 20, 5195–5210.
Cortés JCG, Carnero E, Ishiguro J, Sánchez Y, Durán A, Ribas JC (2005). The novel fission yeast (1,3)β-D-glucan synthase catalytic subunit Bgs4p is essential during both cytokinesis and polarized growth. J Cell Sci 118, 157–174.
Cortés JCG, Konomi M, Martins IM, Muñoz J, Moreno MB, Osumi M, Durán A, Ribas JC (2007). The (1,3)β-d-glucan synthase subunit Bgs1p is responsible for the fission yeast primary septum formation. Mol Microbiol 65, 201–217.
Cortés JCG, Pujol N, Sato M, Pinar M, Ramos M, Moreno B, Osumi M, Ribas JC, Pérez P (2015). Cooperation between Paxillin-like protein Pxl1 and glucan synthase Bgs1 is essential for actomyosin ring stability and septum formation in fission yeast. PLoS Genet 11, e1005358.
Cortés JCG, Sato M, Muñoz J, Moreno MB, Clemente-Ramos JA, Ramos M, Okada H, Osumi M, Durán A, Ribas JC (2012). Fission yeast Ags1 confers the essential septum strength needed for safe gradual cell abscission. J Cell Biol 198, 637–656.
Davidson R, Laporte D, Wu J-Q (2015). Regulation of Rho-GEF Rgf3 by the arrestin Art1 in fission yeast cytokinesis. Mol Biol Cell 26, 453–466.
Davies T, Jordan SN, Chand V, Sees JA, Laband K, Carvalho AX, Shirasu-Hiza M, Kovar DR, Dumont J, Canman JC (2014). High-resolution temporal analysis reveals a functional timeline for the molecular regulation of cytokinesis. Dev Cell 30, 209–223.
Dey SK, Pollard TD (2018). Involvement of the septation initiation network in events during cytokinesis in fission yeast. J Cell Sci 131, jcs216895.
Edelstein AD, Tsuchida MA, Amodaj N, Pinkard H, Vale RD, Stuurman N (2014). Advanced methods of microscope control using μManager software. J Biol Methods 1, e10.
El-Amine N, Carim SC, Wernike D, Hickson GRX (2019). Rho-dependent control of the Citron kinase, Sticky, drives midbody ring maturation. Mol Biol Cell 30, 2185–2204.
Fernandez R, Berro J (2016). Use of a fluoride channel as a new selection marker for fission yeast plasmids and application to fast genome editing with CRISPR/Cas9. Yeast 33, 549–557.
Grallert A, Krapp A, Bagley S, Simanis V, Hagan IM (2004). Recruitment of NIMA kinase shows that maturation of the *S. pombe* spindle-pole body occurs over consecutive cell cycles and reveals a role for NIMA in modulating SIN activity. Genes Dev 18, 1007–1021.
Hachet O, Simanis V (2008). Mid1p/anillin and the septation initiation network orchestrate contractile ring assembly for cytokinesis. Genes Dev 22, 3205–3216.
Janson ME, Setty TG, Paoletti A, Tran PT (2005). Efficient formation of bipolar microtubule bundles requires microtubule-bound γ-tubulin complexes. J Cell Biol 169, 297–308.
Kono K, Saeki Y, Yoshida S, Tanaka K, Pellman D (2012). Proteasomal degradation resolves competition between cell polarization and cellular wound healing. Cell 150, 151–164.
Laplante C, Berro J, Karatekin E, Hernandez-Leyva A, Lee R, Pollard TD (2015). Three myosins contribute uniquely to the assembly and constriction of the fission yeast cytokinetic contractile ring. Curr Biol 25, 1955–1965.
Leong SL, Lynch EM, Zou J, Tay YD, Borek WE, Tuijtel MW, Rappsilber J, Sawin KE (2019). Reconstitution of microtubule nucleation *in vitro* reveals novel roles for Mzt1. Curr Biol 29, 2199–2207.e10.
Li Y, Christensen JR, Homa KE, Hocky GM, Fok A, Sees JA, Voth GA, Kovar DR (2016). The F-actin bundler α-actinin Ain1 is tailored for ring assembly and constriction during cytokinesis in fission yeast. Mol Biol Cell 27, 1821–1833.
Li H, Handsaker B, Wysoker A, Fennell T, Ruan J, Homer N, Marth G, Abecasis G, Durbin R, 1000 Genome Project Data Processing Subgroup (2009). The sequence alignment/map format and SAMtools. Bioinformatics 25, 2078–2079.
Liu J, Wang H, McCollum D, Balasubramanian MK (1999). Drc1p/Cps1p, a 1,3-β-glucan synthase subunit, is essential for division septum assembly in *Schizosaccharomyces pombe*. Genetics 153, 1193–1203.
Lock A, Rutherford K, Harris MA, Hayles J, Oliver SG, Bahler J, Wood V (2019). PomBase 2018: user-driven reimplementation of the fission yeast database provides rapid and intuitive access to diverse, interconnected information. Nucleic Acids Res 47, D821–D827.
Loo T-H, Balasubramanian M (2008). *Schizosaccharomyces pombe* Pak-related protein, Pak1p/Orb2p, phosphorylates myosin regulatory light chain to inhibit cytokinesis. J Cell Biol 183, 785–793.
Maundrell K (1990). nmt1 of fission yeast. A highly transcribed gene completely repressed by thiamine. J Biol Chem 265, 10857–10864.
Michaelson D, Silletti J, Murphy G, D'Eustachio P, Rush M, Philips MR (2001). Differential localization of Rho GTPases in live cells: regulation by hypervariable regions and RhoGDI binding. J Cell Biol 152, 111–126.
Minet M, Nurse P, Thuriaux P, Mitchison JM (1979). Uncontrolled septation in a cell division cycle mutant of the fission yeast *Schizosaccharomyces pombe*. J Bacteriol 137, 440–446.
Mitchison JM, Nurse P (1985). Growth in cell length in the fission yeast *Schizosaccharomyces pombe*. J Cell Sci 75, 357–376.
Moreno S, Klar A, Nurse P (1991). Molecular genetic analysis of fission yeast *Schizosaccharomyces pombe*. Meth Enzymol 194, 795–823.
Morris Z, Sinha D, Poddar A, Morris B, Chen Q (2019). Fission yeast TRP channel Pkd2p localizes to the cleavage furrow and regulates cell separation during cytokinesis. Mol Biol Cell 30, 1791–1804.
Murray JM, Watson AT, Carr AM (2016). Transformation of *Schizosaccharomyces pombe*: lithium acetate/dimethyl sulfoxide procedure. Cold Spring Harbor Protocols 2016, pdb.prot090969.
Nakano K, Arai R, Mabuchi I (1997). The small GTP-binding protein Rho1 is a multifunctional protein that regulates actin localization, cell polarity, and septum formation in the fission yeast *Schizosaccharomyces pombe*. Genes Cells 2, 679–694.
Okada H, Wloka C, Wu J-Q, Bi E (2019). Distinct roles of Myosin-II isoforms in cytokinesis under normal and stressed conditions. iScience 14, 69–87.
Pardo M, Nurse P (2003). Equatorial retention of the contractile actin ring by microtubules during cytokinesis. Science 300, 1569–1574.
Pelham RJ, Chang F (2002). Actin dynamics in the contractile ring during cytokinesis in fission yeast. Nature 419, 82–86.
Pollard TD (2017). Nine unanswered questions about cytokinesis. J Cell Biol 216, 3007–3016.
Proctor SA, Minc N, Boudaoud A, Chang F (2012). Contributions of turgor pressure, the contractile ring, and septum assembly to forces in cytokinesis in fission yeast. Curr Biol 22, 1601–1608.
Pronobis MI, Deuitch N, Peifer M (2016). The Miraprep: A protocol that uses a Miniprep kit and provides Maxiprep yields. PLoS One 11, e0160509.
R Core Team (2018). R: a language and environment for statistical computing. R Foundation for Statistical Computing.
Roberts-Galbraith RH, Chen J-S, Wang J, Gould KL (2009). The SH3 domains of two PCH family members cooperate in assembly of the *Schizosaccharomyces pombe* contractile ring. J Cell Biol 184, 113–127.
Roberts-Galbraith RH, Ohi MD, Ballif BA, Chen J-S, McLeod I, McDonald WH, Gygi SP, Yates JR, Gould KL (2010). Dephosphorylation of F-BAR protein Cdc15 modulates its conformation and stimulates its scaffolding activity at the cell division site. Mol Cell 39, 86–99.
Robinson JT, Thorvaldsdóttir H, Wenger AM, Zehir A, Mesirov JP (2017). Variant review with the Integrative Genomics Viewer. Cancer Res 77, e31—e34.
Samejima I, Lourenco PCC, Snaith HA, Sawin KE (2005). Fission yeast Mto2p regulates microtubule nucleation by the centrosomin-related protein Mto1p. Mol Biol Cell 16, 3040–3051.
Samejima I, Miller VJ, Rincón SA, Sawin KE (2010). Fission yeast Mto1 regulates diversity of cytoplasmic microtubule organizing centers. Curr Biol 20, 1959–1965.

Sawin KE, Lourenco PCC, Snaith HA (2004). Microtubule nucleation at non-spindle pole body microtubule-organizing centers requires fission yeast centrosomin-related protein mod20p. Curr Biol 14, 763–775.
Sawin KE, Tran PT (2006). Cytoplasmic microtubule organization in fission yeast. Yeast 23, 1001–1014.
Schindelin J, Arganda-Carreras I, Frise E, Kaynig V, Longair M, Pietzsch T, Preibisch S, Rueden C, Saalfeld S, Schmid B, *et al*. (2012). Fiji: an open-source platform for biological-image analysis. Nat Meth 9, 676–682.
Sethi K, Palani S, Cortés JCG, Sato M, Sevugan M, Ramos M, Vijaykumar S, Osumi M, Naqvi NI, Ribas JC, Balasubramanian M (2016). A new membrane protein Sbg1 links the contractile ring apparatus and septum synthesis machinery in fission yeast. PLoS Genet 12, e10063830.
Simanis V (2015). Pombe's thirteen—control of fission yeast cell division by the septation initiation network. J Cell Sci 128, 1465–1474.
Sohrmann M, Schmidt S, Hagan I, Simanis V (1998). Asymmetric segregation on spindle poles of the *Schizosaccharomyces pombe* septum-inducing protein kinase Cdc7p. Genes Dev 12, 84–94.
Tatebe H, Goshima G, Takeda K, Nakagawa T, Kinoshita K, Yanagida M (2001). Fission yeast living mitosis visualized by GFP-tagged gene products. Micron 32, 67–74.
Tebbs IR, Pollard TD (2013). Separate roles of IQGAP Rng2p in forming and constricting the *Schizosaccharomyces pombe* cytokinetic contractile ring. Mol Biol Cell 24, 1904–1917.
Thévenaz P, Ruttimann UE, Unser M (1998). A pyramid approach to subpixel registration based on intensity. IEEE Trans Image Process 7, 27–41.
Thiyagarajan S, Munteanu EL, Arasada R, Pollard TD, O'Shaughnessy B (2015). The fission yeast cytokinetic contractile ring regulates septum shape and closure. J Cell Sci 128, 3672–3681.
Vavylonis D, Wu J-Q, Hao S, O'Shaughnessy B, Pollard TD (2008). Assembly mechanism of the contractile ring for cytokinesis by fission yeast. Science 319, 97–100.
Venkatram S, Jennings JL, Link A, Gould KL (2005). Mto2p, a novel fission yeast protein required for cytoplasmic microtubule organization and anchoring of the cytokinetic actin ring. Mol Biol Cell 16, 3052–3063.
Wachtler V, Huang Y, Karagiannis J, Balasubramanian MK (2006). Cell cycle-dependent roles for the FCH-domain protein Cdc15p in formation of the actomyosin ring in *Schizosaccharomyces pombe*. Mol Biol Cell 17, 3254–3266.
Walker BJ, Abeel T, Shea T, Priest M, Abouelliel A, Sakthikumar S, Cuomo CA, Zeng Q, Wortman J, Young SK, Earl AM (2014). Pilon: an integrated tool for comprehensive microbial variant detection and genome assembly improvement. PLoS One 9, e112963.
Wang N, Lo Presti L, Zhu Y-H, Kang M, Wu Z, Martin SG, Wu J-Q (2014). The novel proteins Rng8 and Rng9 regulate the myosin-V Myo51 during fission yeast cytokinesis. J Cell Biol 205, 357–375.
Wickham H (2017). tidyverse: easily install and load the "tidyverse."
Wood V, Gwilliam R, Rajandream M-A, Lyne M, Lyne R, Stewart A, Sgouros J, Peat N, Hayles J, Baker S, *et al*. (2002). The genome sequence of *Schizosaccharomyces pombe*. Nature 415, 871–880.
Wu J-Q, Kuhn JR, Kovar DR, Pollard TD (2003). Spatial and temporal pathway for assembly and constriction of the contractile ring in fission yeast cytokinesis. Dev Cell 5, 723–734.
Wu J-Q, Pollard TD (2005). Counting cytokinesis proteins globally and locally in fission yeast. Science 310, 310–314.
Yamashita A, Sato M, Fujita A, Yamamoto M, Toda T (2005). The roles of fission yeast ase1 in mitotic cell division, meiotic nuclear oscillation, and cytokinesis checkpoint signaling. Mol Biol Cell 16, 1378–1395.
Zhang W, Yu Y, Hertwig F, Thierry-Mieg J, Zhang W, Thierry-Mieg D, Wang J, Furlanello C, Devanarayan V, Cheng J, *et al*. (2015). Comparison of RNA-seq and microarray-based models for clinical endpoint prediction. Genome Biol 16, 133.
Zhou Z, Munteanu EL, He J, Ursell T, Bathe M, Huang KC, Chang F (2015). The contractile ring coordinates curvature-dependent septum assembly during fission yeast cytokinesis. Mol Biol Cell 26, 78–90.
Zhurinsky J, Salas-Pino S, Iglesias-Romero AB, Torres-Mendez A, Knapp B, Flor-Parra I, Wang J, Bao K, Jia S, Chang F, Daga RR. (2019). Effects of the microtubule nucleator Mto1 on chromosomal movement, DNA repair, and sister chromatid cohesion in fission yeast. Mol Biol Cell 30, 2695–2708.
Zimmerman S, Chang F (2005). Effects of γ-tubulin complex proteins on microtubule nucleation and catastrophe in fission yeast. Mol Biol Cell 16, 2719–2733.
Zimmerman S, Daga RR, Chang F (2004). Intra-nuclear microtubules and a mitotic spindle orientation checkpoint. Nat Cell Biol 6, 1245–1246.